

This item was submitted to [Loughborough's Research Repository](#) by the author.  
Items in Figshare are protected by copyright, with all rights reserved, unless otherwise indicated.

## Investigation of microstructural evolution and creep rupture behaviour of 9% Cr MarBN steel welds

PLEASE CITE THE PUBLISHED VERSION

<https://doi.org/10.1016/j.msea.2020.139546>

PUBLISHER

Elsevier BV

VERSION

AM (Accepted Manuscript)

PUBLISHER STATEMENT

This paper was accepted for publication in the journal Materials Science and Engineering: A and the definitive published version is available at <https://doi.org/10.1016/j.msea.2020.139546>

LICENCE

CC BY-NC-ND 4.0

REPOSITORY RECORD

Xu, X, A Benaarbia, D Allen, Mark Jepson, and W Sun. 2020. "Investigation of Microstructural Evolution and Creep Rupture Behaviour of 9% Cr Marbn Steel Welds". Loughborough University.  
<https://hdl.handle.net/2134/12436424.v1>.

# **Investigation of microstructural evolution and creep rupture behaviour of 9% Cr MarBN steel welds**

X. Xu<sup>\*1</sup>, A. Benaarbia<sup>2</sup>, D. Allen<sup>1</sup>, Mark A. E. Jepson<sup>1</sup>, W. Sun<sup>3</sup>

<sup>1</sup> Department of Materials, Loughborough University, Loughborough, Leicestershire  
LE11 3TU, UK

<sup>2</sup> Arts et Métiers, CNRS, Université de Lorraine, LEM3, F-57000 Metz, France

<sup>3</sup> Department of Mechanical, Materials and Manufacturing Engineering, University of  
Nottingham, Nottingham, Nottinghamshire, NG7 2RD, UK

## **ABSTRACT**

The weldments made from the 9-12% Cr tempered martensitic steel are associated with a complex microstructure arising from complicated thermal histories of the fusion and heat affected zones. The complicated microstructural and micro-mechanical states in these critical regions provide a challenge for the determination of creep failure mechanisms. Based on detailed metallographic examination, the microstructural distribution in the heat affected zone of the welds constructed using a recently developed 9% Cr MarBN steel, IBN-1, has been identified and classified into Equiaxed Zone (EZ), Duplex Zone (DZ) and Over-tempered Zone (OZ). Cross-weld testing performed at 650°C has revealed a significant reduction in creep life as compared to bulk material. Creep rupture has been shown to occur in the parent metal region with a ductile manner at a high stress, whereas creep rupture initiates in the DZ region in an intergranular manner at a low stress. Detailed metallographic investigation has further revealed a higher damage susceptibility in the regions along the pre-existing Prior Austenite Grain Boundaries (PAGBs). The diffusional reaustenitisation of local microstructure along the PAGBs leads to a lower strength of matrix in combination with a lack of intergranular

precipitates as compared to the surrounding microstructure formed after displacive  
reaustenitisation.

**KEYWORDS:** 9% Cr tempered martensitic steel; heat affected zone; multi-pass welding;  
high temperature creep; failure mechanism

## **1. INTRODUCTION**

The 9-12% Cr creep resistant martensitic steels are widely used in high temperature  
pressure vessels and piping for the power generation industry due to their good  
combination of creep strength and oxidation resistance. Based on a nominal composition  
of Fe-9%Cr-3%W-3%Co-VNbBN [1], variants of Martensitic steel strengthened by  
boron and nitrogen (MarBN) have been recently developed to replace the more  
conventional 9% Cr materials such as the Grade 91 and 92 steels by providing superior  
creep performance in combination with sufficient oxidation resistance [2]. During recent  
years, the major developments based on the concept of MarBN include a range of  
materials originating from international collaborative research activities including the  
G115 (China), SAVE12AD (Japan), NPM-1 (Europe) and the IBN-1 (UK) steels [3–6].  
These materials are typically manufactured by using common industrial processes  
finished with normalisation and tempering to produce a tempered martensitic  
microstructure in combination with secondary precipitates distributed both on grain  
boundaries and within the grain interiors [1]. These MarBN steels are also compatible  
with a variety of fusion welding processes including Manual Metal Arc Welding  
(MMAW), Submerged Arc Welding (SAW) and Gas Tungsten Arc Weld (GTAW).  
Multi-pass welding processes have been used to fabricate welds on MarBN steels to  
achieve sufficient ductility in the weld metal and the Heat Affected Zone (HAZ).

Interest in the creep performance of welds fabricated in 9-12% Cr steels is increasing due to their potential applications in power plant systems. The evaluation of welded joint behaviour during creep exposure is a key factor in determining the lifetime of power plant components. The existing studies of cross-weld samples under creep conditions have shown that the ratio of creep rupture strength between cross-welds and the parent material depends on both creep loading conditions and welding procedure [7]. At low testing temperatures there is no large difference between parent metal and cross-weld creep strength, whilst this difference becomes important at high temperatures and low stress levels [7]. Additionally, rupture locations were found to shift from the weld metal to the HAZ as the applied stress decreased [8]. No substantial differences were found in the minimum creep rate, the time to fracture and creep ductility for the cross-weld specimens taken from different locations of the weld [8].

The welds fabricated in 9-12% Cr steels are associated with premature creep failure within the HAZ, typically termed as 'Type IV' failure [9]. Type IV failure is commonly presented in the HAZ region close to the boundary with the parent metal and causes a substantial loss in creep strength for weldments as compared to bulk materials [10,11]. Detailed metallographic examination conducted on interrupted creep test specimens has revealed the presence of creep cavities prior to final rupture in a Type IV manner [12]. Based on extensive metallographic examination, the metallurgical cause for the formation of creep cavities is complicated and linked with a range of factors relating to the microstructure of 9-12% Cr steels. For instance, the presence of second phase particles (e.g. boron nitride, BN) above a critical size has been determined as a critical issue that promotes the formation of cavities from the early stage of creep [12,13]. The presence of Type IV failure in 9-12% Cr steels is also related with a layer of HAZ material exhibiting



a refined martensitic microstructure in combination with a lack of precipitate formation on lath and grain boundaries [14,15]. However, most of the existing studies are conducted using welds made from conventional materials such as Grade 91 and 92 steels, whilst the research focused on the creep failure mechanism of recently developed MarBN steels is comparatively limited.

Detailed investigation of the creep failure mechanism of 9-12% Cr steel welds is also challenging due to a complicated HAZ microstructure formed by the complex thermal distribution established during multi-pass welding. Extensive research has been conducted using experimental measurement and numerical modelling techniques to understand the thermal distribution in the HAZ [16–18]. These studies reveal that the thermal history of the HAZ is typically composed of a heating phase with a heating rate of  $>100^{\circ}\text{C/s}$  and a subsequent cooling phase during which temperature decreases to the ambient level within tens of seconds [16,17]. The variation of the microstructure in the HAZ has been further correlated with thermal distribution based on detailed metallographic examination and dilatometry simulation in 9-12% Cr steels as reported in [19,20]. Detailed previous studies conducted on a more conventional Grade 92 alloy have classified the HAZ microstructure into three critical sub-regions: Completely Transformed Zone (CTZ), Partially Transformed Zone (PTZ) and Over-Tempered Zone (OTZ) based on the range of peak temperatures reached during weld thermal cycles [20]. A more recent study based on the dilatometry simulation of a MarBN steel, IBN-1, has further determined a similar trend of variation in the HAZ microstructure as a function of peak temperature [21]. However, there is a lack of direct, systematic investigations from the weld HAZs to correlate with the presence of creep damage in MarBN steels.

In the current research, the microstructural distribution in the HAZ of multi-pass welds in a parent metal of the MarBN steel, IBN-1, has been investigated in detail in the initial state without creep exposure. The mechanical behaviour of the IBN-1 welds has been further investigated upon short-term creep exposure using cross-weld specimens at 650°C to compare with the bulk materials tested at similar testing conditions. Detailed metallographic examinations have been subsequently performed to identify the critical metallurgical factors related to the formation of creep damage after rupture at different stress levels.

## 2. MATERIAL AND EXPERIMENTAL METHODS

### 2.1. Materials

The chemical composition of the IBN-1 steel used (referred as parent metal) is listed in Table 1. The initial heat treatment of the parent metal involved a normalisation process at 1200°C for 4 hours and a tempering process at 765°C for 3 hours. A butt weld was then fabricated between the plates of parent metal that are ~30 mm in thickness by using a multi-pass MMAW process with a recently developed matching filler material, Metrode® Chromet® 933. In total, 26 weld beads were deposited with a heat input of 1.1 – 1.5 kJ/mm with the interpass temperature maintained between 200°C and 300°C. Post Weld Heat Treatment (PWHT) was conducted after welding at 760°C for 2 hours.

**Table 1. Chemical composition of the IBN-1 parent metal (wt. %, balance is Fe).**

C	Si	Mn	P	S	Cr	Mo	Ni
0.1	0.45	0.54	0.012	0.004	8.74	0.05	0.14
Al	B	Co	Cu	Nb	V	W	N
0.007	0.012	3.02	0.04	0.06	0.21	2.53	0.018

## 2.2. Creep testing

Creep test specimens were machined to a dog-bone shape with a cylindrical gauge portion measuring 50 mm in length and 10 mm in diameter. The gauge portion consists of the weld and the parent metals together with the intermediate HAZ located at ~10 mm from the boundary between the gauge and the head portions, Figure 1.

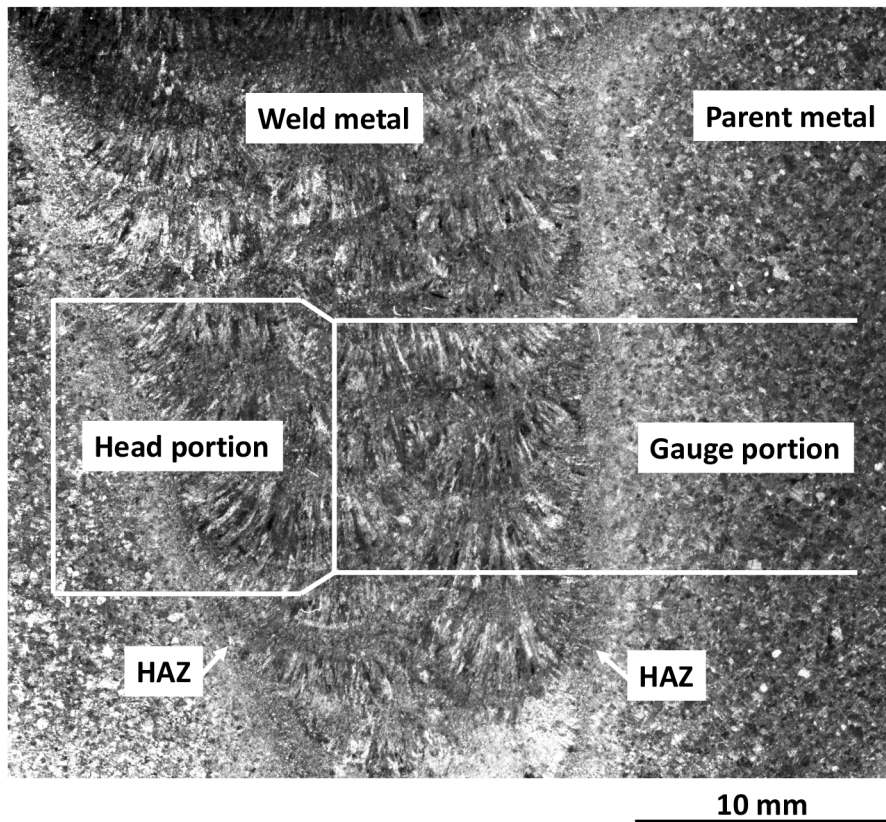


**Figure 1. Optical micrograph giving an overview of the weld structure in the cross-weld creep specimen.**

Isothermal short-term cross-weld creep tests were conducted at 650°C with a series of stress levels ranging from 160 MPa to 280 MPa. The stress levels were selected based on the existing experience of creep testing of MarBN steel [22], such that the specimens were expected to be ruptured in different manners for a comparison in creep characteristics.

The specimens tested at a stress level close to 280 MPa were expected to fracture in a ductile manner with rupture occurring in the parent metal. The specimens tested at a stress level close to 160 MPa were chosen to fracture in the HAZ.

The testing machine was equipped with high temperature Linear Variable Displacement Transformers (LVDT) to continuously monitor the elongation of specimens, and a resistance-heating furnace enabling a quasi-homogeneous testing temperature of up to 800°C. The measured creep strain represents the integral accumulated creep strain of the entire cross-weld material within the gauge length. Three thermocouples were attached to the specimen inside the furnace to track the operating temperature. Note that the thermal gradient between both sample extremities was less than 2°C. Prior to testing, thermal loading was first performed with a rate of 40°C/min until reaching the target temperature. After stabilization of the furnace temperature (~30 minutes), creep tests were conducted until the macroscopic failure of samples.

### **2.3. Metallographic examination**

Gauge portions of the creep ruptured specimens were sectioned from the head and along the longitudinal direction for detailed metallographic examination of the cross-sections. The specimens were prepared using conventional metallographic preparation methods, which involved mounting in electrically conductive Bakelite, grinding on SiC with water to a 1200 grit finish, polishing on standard polishing cloths using 6 µm and 1 µm diamond suspensions and a final chemo-mechanical polishing process using a suspension of 0.06 µm colloidal silica in water. An as-fabricated weld was also prepared using the same procedure to provide details of the initial microstructure before creep exposure.

Hardness testing was conducted on the as-fabricated weld using a loading weight of 10 kg and a dwell time of 10 s using a Struers® Durascan® 70 hardness testing system equipped with a Vickers indenter. Seven individual measurements were conducted to obtain the average value of hardness from both the weld and the parent metals. Hardness mapping was also undertaken on the as-fabricated weld and on creep ruptured specimens in the regions adjacent to the rupture surface using a loading weight of 0.2 kg and a dwell time of 10 s using the identical hardness testing system. Vickers hardness indents were distributed on a square grid with a spacing of 0.1 mm.

Fractography examination was performed on the fracture surfaces of creep ruptured specimens using a JEOL® JSM-7800F Field Emission Gun (FEG) Scanning Electron Microscope (SEM) at an accelerating voltage of 5 kV. Grain orientation mapping of the matrix was undertaken by performing EBSD mapping at an accelerating voltage of 20 kV using an Oxford Instruments® Nordlys® MAX<sup>2</sup> camera in the JEOL® JSM-7800F FEG-SEM. EBSD maps were collected on the cross-section of the as-fabricated weld and adjacent to the rupture surface of creep fractured specimens at a step size of 2 µm with a size of 1000 × 1000 µm to provide an overview of the microstructure. EBSD mapping was also performed at a finer step size of 0.1 µm to obtain details of the microstructure. The distribution of secondary precipitates in identical regions to where EBSD mapping was conducted was characterised using ion induced Secondary Electron (SE) imaging in a FEI® Nova Nanolab® 600 Focused Ion Beam (FIB) FEG-SEM. The ion beam was operated at an accelerating voltage of 30 kV with XeF<sub>2</sub> gas etching used to enhance the contrast differential between precipitates and matrix [19,23].

Thin-foil specimens were extracted from site-specific locations where the correlative EBSD/ion induced SE analysis was conducted using an *in-situ* lift-out technique [24] in

a FEI® Nova Nanolab® 600 FIB/FEG-SEM. The thinning of specimens was performed at an accelerating voltage of 30 kV with a beam current decreasing to 0.1 nA, followed by a final cleaning process performed at an accelerating voltage of 5 kV. The extracted thin-foil specimens were investigated using Bright Field Scanning Transmission Electron Microscopy (BF-STEM) in a FEI® Tecnai® F20 Transmission Electron Microscope (TEM) at an accelerating voltage of 200 kV. Secondary precipitates were further characterised using Selected Area Electron Diffraction (SAED) in combination with Energy Dispersive X-ray (EDX) spectroscopy using an Oxford Instruments® X-Max 80<sup>N</sup> TLE EDX system.

### **3. RESULTS**

#### **3.1. Microstructural distribution in the as-fabricated condition**

The hardness of the weld and the parent metals were measured using macro-hardness testing. The hardness of the weld and the parent metals were determined to be  $290 \pm 4$  and  $249 \pm 2$  HV<sub>10</sub>, respectively. The value of hardness obtained from the parent metal is consistent with the previous reports from similar MarBN steels [25,26]. The weld metal exhibited a higher level of hardness as compared to the parent metal. This is possibly attributed to a more refined martensitic microstructure as formed in the weld metal after rapid solidification and cooling during the welding stage, and a less homogenised and recovered martensitic substructure due to a lack of normalisation treatment as compared to the parent metal.

The microstructural variation in the as-fabricated weld without creep exposure was further characterised using hardness mapping analysis at a different loading weight of 0.2

kg. Figure 2 demonstrates a macro optical micrograph providing an overview of the weld microstructure and a hardness map from the same region.

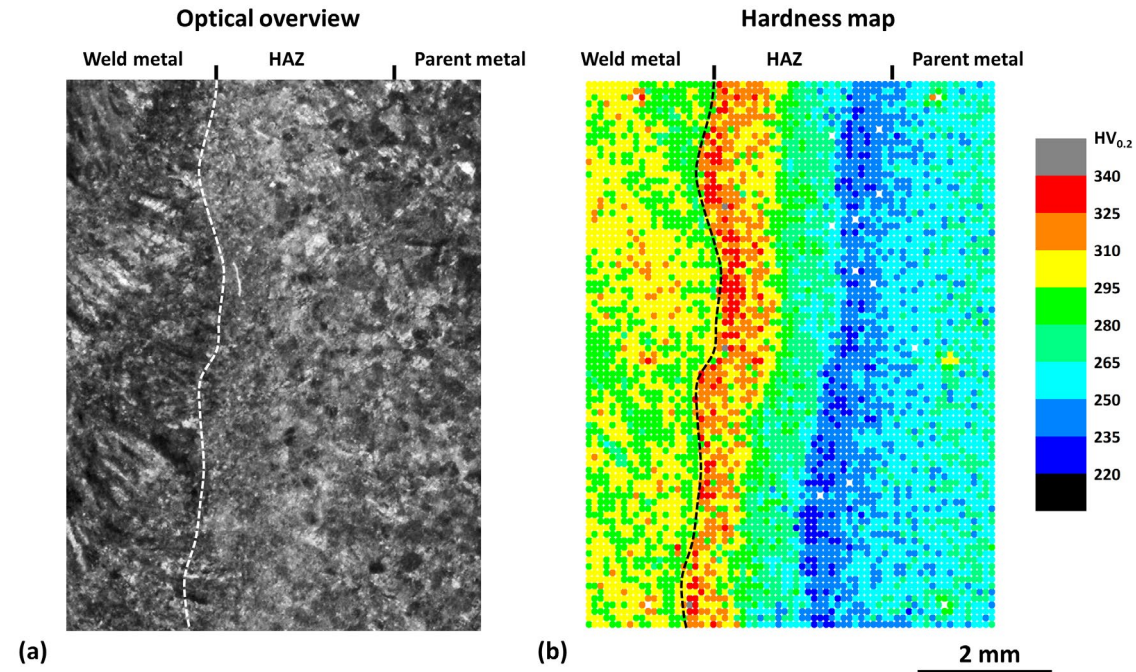


**Figure 2. (a) A macro optical micrograph demonstrating the variation of microstructure between the weld metal, the HAZ and the parent metal. (b) A hardness map showing the variation in hardness from the same region.**

Based on the hardness map, the weld metal has a higher level of hardness at  $296 \pm 9 \text{ HV}_{0.2}$  as compared to the parent metal measured with a hardness of  $261 \pm 9 \text{ HV}_{0.2}$ . These values of hardness are lower than the values obtained at a loading weight of 10 kg. This is attributable to the different measuring volumes that were achieved at a different loading weight. No significant variation in hardness was observed in the HAZ along the direction parallel to the fusion boundary (i.e. from bottom to top in Figure 2), whilst a decrease in hardness was clearly observed as the distance from the fusion boundary increased.

The distribution in hardness in the HAZ region suggests significant microstructural variation as a function of distance from the fusion boundary. Correlative EBSD analysis was further conducted to detail the microstructural gradient in the HAZ, Figure 3.

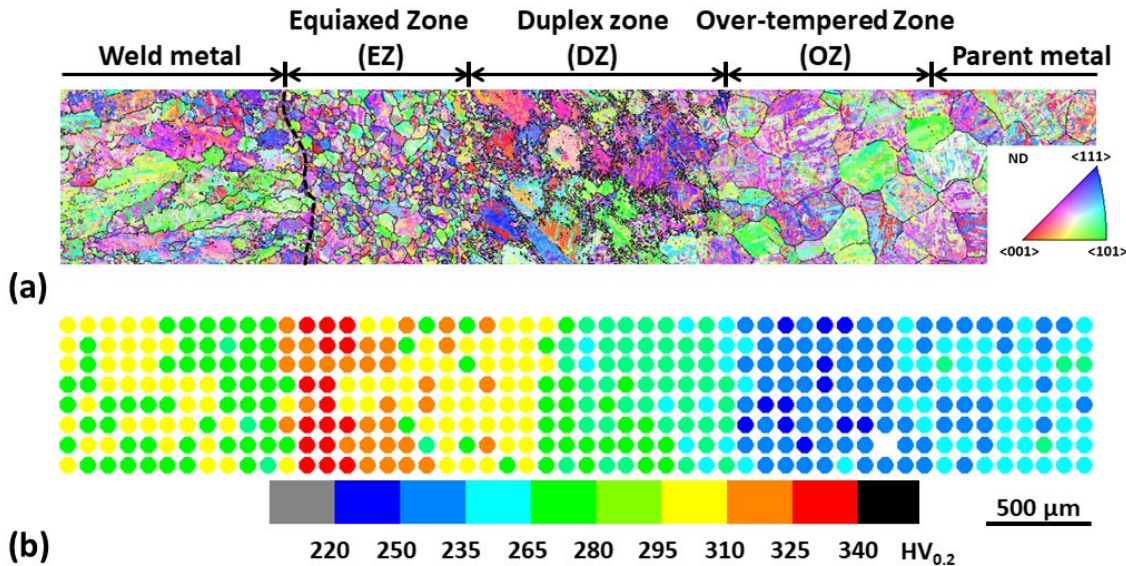


**Figure 3. (a) An EBSD map providing an overview of the tempered martensitic matrix in as-fabricated IBN-1 weld. The grain boundaries with a misorientation range between 20° and 50° are outlined by solid lines. (b) A correlative hardness map showing the variation of hardness in the identical region is also included for comparison.**

Due to a Kurdjumov-Sachs orientation relationship preserved between the martensitic ( $\alpha'$ ) and the parental austenitic ( $\gamma$ ) phases during martensitic transformation, the austenitic grain structure was characterised from EBSD maps using a boundary misorientation range between 20° and 50° [20,27,28]. Figure 3a shows that columnar and equiaxed austenitic structures are presented in the weld and the parent metals, respectively. The columnar grains in the weld metal are typically 50-200 μm in width and over 1000 μm in length, whilst the equiaxed grains in the parent metal are predominantly 100-500 μm in



diameter. In the HAZ region close to the fusion boundary, the grain structure was found to have transformed from a refined, equiaxed morphology in the region <1 mm from the fusion boundary to a duplex grain structure containing small austenite grain ‘necklaces’ around pre-existing PAGBs in the region 1-2 mm from the fusion boundary. The equiaxed grains in the region <1 mm from the fusion boundary are predominantly <150  $\mu\text{m}$  in diameter, whereas the austenite “necklace” grains on the initial PAGBs are <20  $\mu\text{m}$  in diameter in the regions 1-2 mm from the fusion boundary. The microstructural gradient in the HAZ was further correlated with the variation in hardness as demonstrated in Figure 3b. The hardness map demonstrates that the region with a refined, equiaxed grain structure has a higher level of hardness measuring  $305 \pm 16 \text{ HV}_{0.2}$ , whereas the region showing a duplex grain structure has a lower level of hardness of  $262 \pm 17 \text{ HV}_{0.2}$ . The grain structure in the regions ~2-3 mm from the fusion boundary is not significantly varied from the parent metal, whereas the hardness was lower with an average value measuring  $247 \pm 9 \text{ HV}_{0.2}$ .

The microstructure in the HAZ of as-fabricated IBN-1 weld is further correlated with the microstructure produced by the simulation of weld thermal cycles as previously reported in [21], Table 2.

**Table 2. A comparison in microstructure between the HAZ of the as-fabricated IBN-1 weld and the simulated HAZ material produced using dilatometry-based simulations of weld thermal cycle [21].**

Simulated HAZ material [21]		As-fabricated weld		Classification
Peak temperature	Characteristics of microstructure	Distance from fusion boundary	Characteristics of microstructure	
>1200°C	Equiaxed morphology, grain size <100 $\mu\text{m}$ ;	<1 mm	Equiaxed morphology, grain size <150 $\mu\text{m}$ ;	Equiaxed Zone (EZ)

1000 - 1200°C	Duplex microstructure characterised by refined grains on the pre-existing PAGBs;	1 - 2 mm	Duplex microstructure characterised by small grains (<20 µm) on the pre-existing PAGBs;	Duplex Zone (DZ)
<1000°C	Equiaxed morphology, grain size >300 µm;	2 - 3 mm	Equiaxed morphology, grain size 100 - 500 µm;	Over-tempered Zone (OZ)

245

246 Table 2 demonstrates that the distribution of HAZ microstructure as a function of the  
247 distance from fusion boundary is in strong agreement with the microstructure in the HAZ  
248 simulated materials as a function of peak temperature. Based on the characteristics of  
249 grain structure, the weld HAZ was classified as three critical sub-regions, the Equiaxed  
250 Zone (EZ), the Duplex Zone (DZ) and the Over-tempered Zone (OZ) (Table 2). As  
251 described above, the microstructure in the EZ region is characteristic of refined, equiaxed  
252 grain morphology, whilst the DZ region exhibits a duplexed grain structure containing  
253 the ‘necklaces’ of refined grains on the matrix composed of coarser grains. The  
254 microstructure in the OZ region is not significantly varied from the parent metal. A  
255 detailed description of the microstructure in these sub-regions is not the focus of the  
256 investigation in the current research, as this has been reported elsewhere in a previous  
257 study [21]. However, it has been clearly demonstrated in the current research that the  
258 microstructure of the HAZ in MarBN steel welds is different from the conventional  
259 understanding of the HAZs in low alloy Cr-Mo steels, which are commonly classified  
260 into Coarse-grain (CG), Fine-grain (FG), Inter-critical (IC) and Over-tempered (OT)  
261 regions [11]. In addition, the HAZ of the IBN-1 MarBN steel appears to be different from  
262 the precedent 9% Cr steels as reported in the previous studies [19,20]. The difference  
263 is evidenced by the presence of a duplex grain structure in the DZ regions, which was not  
264 observed in the HAZ of the welds constructed by using Grade 92 steel [19,20].

### 3.2 Mechanical behaviour

Creep responses for cross-weld specimens are compared with the parent metal specimens as previously reported in [22], Figure 4. The corresponding creep properties are summarised in Table 3. These include the Steady-State Creep Rate (SSCR), the time to fracture  $\tau_f$ , ductility  $\epsilon_f$ , and the Reduction of Area (RA).

It can be seen that the three typical creep stages (a primary creep stage followed by an apparently steady-state creep deformation and an accelerating tertiary creep stage) are clearly visible for all tests under investigation. The creep results demonstrate that the minimum creep strain rate increases with the increase of stress while creep rupture time decreases as stress increased. At the medium stress level of 200 MPa and 220 MPa, SSCR values for cross-weld are 26-fold higher than the parent metal, whilst the time to rupture is 14- to 18-fold shorter as compared to the parent metal. This clearly indicates a lower creep resistance of the cross-weld specimen as compared to the parent metal specimen. This finding applies to all stress levels selected for this investigation. Moreover, no significant changes have been observed when comparing both values of the area reduction and ductility reported for both parent metal and cross-weld.

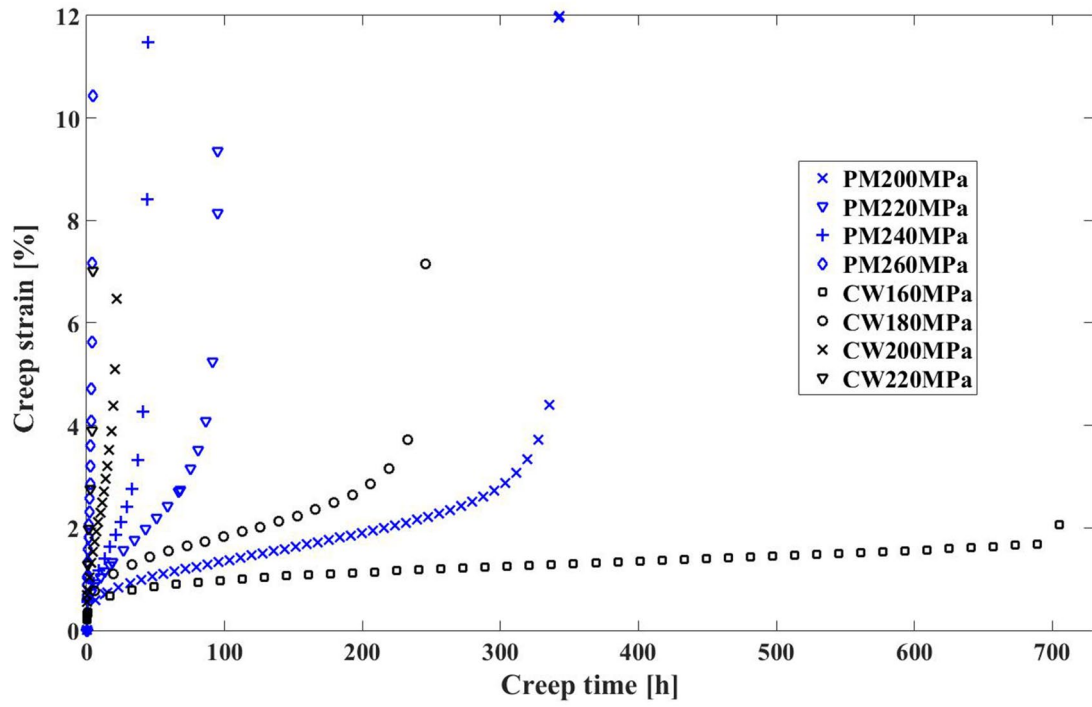
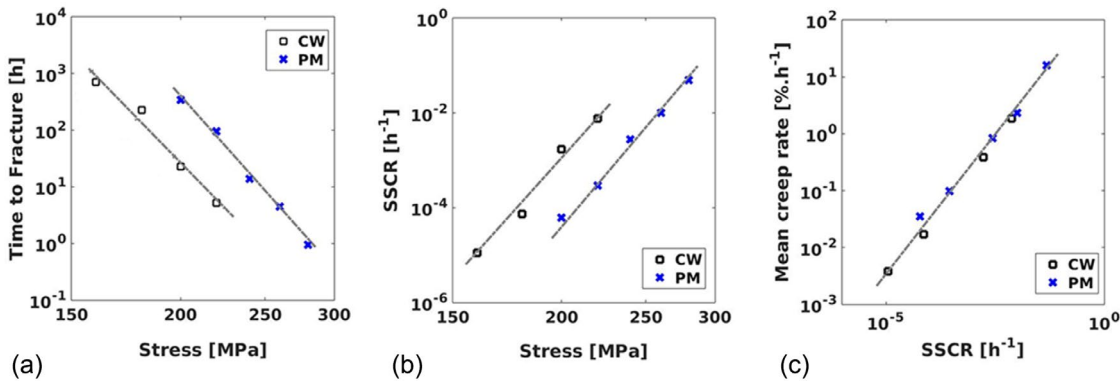


Figure 4. Strain-time curves for creep tests conducted on parent metal (PM) and cross-weld (CW) specimens at 650°C.

Table 3. Material creep properties for parent metal (PM) and cross-weld (CW) specimens selected at different stress levels.

$\sigma$ [MPa]	Material	SSCR [ $10^{-5} \times h^{-1}$ ]	$\tau_f$ [h]	$\epsilon_f$ [%]	RA [%]
160	PM	-	-	-	-
	CW	1.13	705.56	2.66	14.44
180	PM	-	-	-	-
	CW	7.31	248.35	5.62	42.24
200	PM	6.12	342.91	11.93	62.05
	CW	170.02	22.96	7.86	73.79
220	PM	29.12	95.47	9.36	73.68
	CW	770.15	5.14	11.35	80.29
240	PM	280.32	13.73	11.48	74.29
	CW	-	-	-	-
260	PM	1000.21	4.43	10.48	75.11
	CW	-	-	-	-
280	PM	4851.23	0.94	14.88	81.08
	CW	-	-	-	-

All aforementioned creep rupture characteristics of the parent metal and cross-weld are gathered for comparison in Figure 5 and summarised in Table 4 in the form of power-law (relating the time-to-rupture or SSCR to the stress) and Monkman-Grant (relating the mean creep rate to SSCR) relationships. Figures 5a and 5b show that the cross-weld specimens have a considerably shorter creep life and a higher creep strain rate as compared to the parent metal specimens, whilst Figure 5c reveals a similar Monkman-Grant (MG) relationship for both the cross-weld and the parent metal specimens. In addition, no significant differences were observed for the apparent stress and MG exponents between the cross-weld and the parent metal specimens, as detailed in Table 4. The parent metal specimens show a slightly higher stress exponent value  $m$  as compared to the cross-weld specimen, whilst the stress exponent value  $n$  is slightly higher for the cross-weld specimen. The MG exponent,  $\xi$ , for the cross-weld specimens turns out to be 0.95, whilst that of the parent metal specimens is  $\sim 0.87$ .



**Figure 5. (a) Time to fracture vs. applied stress. (b) SSCR vs. applied stress. (c) Mean creep rate ( $\epsilon_f/\tau_f$ ) vs. SSCR of IBN-1 cross-weld (CW) and parent metal (PM) specimens.**

**Table 4. Apparent values of creep function coefficients for parent metal (PM) and cross-weld (CW) specimens.**

Material	Time to fracture $\tau_f = p \sigma^{-m}$		Steady-state creep rate $SSCR = q \sigma^n$		Monkman-Grant relationship $SSCR^\xi = \omega \epsilon_f / \tau_f$	
	$p$ [(MPa) <sup>-1</sup> .h]	$m$ [-]	$q$ [(MPa.h) <sup>-1</sup> ]	$n$ [-]	$\omega$ [-]	$\xi$ [-]
PM	$7.59 \times 10^{42}$	17.53	$1.07 \times 10^{-50}$	19.88	0.63	0.87
CW	$2.63 \times 10^{38}$	16.08	$6.47 \times 10^{-53}$	21.42	0.56	0.95

306

### 307 3.3. Creep rupture behaviour of cross-weld specimen at different stress levels

308 The microstructures in the creep exposed cross-weld specimens were investigated using  
 309 hardness mapping analysis in combination with fractography examination to understand  
 310 the correlation between the weld microstructure and the creep rupture behaviour.

311 Hardness mapping was conducted in the region close to the rupture surface to reveal the  
 312 variation in hardness after creep testing at 650°C and 160 MPa, Figure 6.

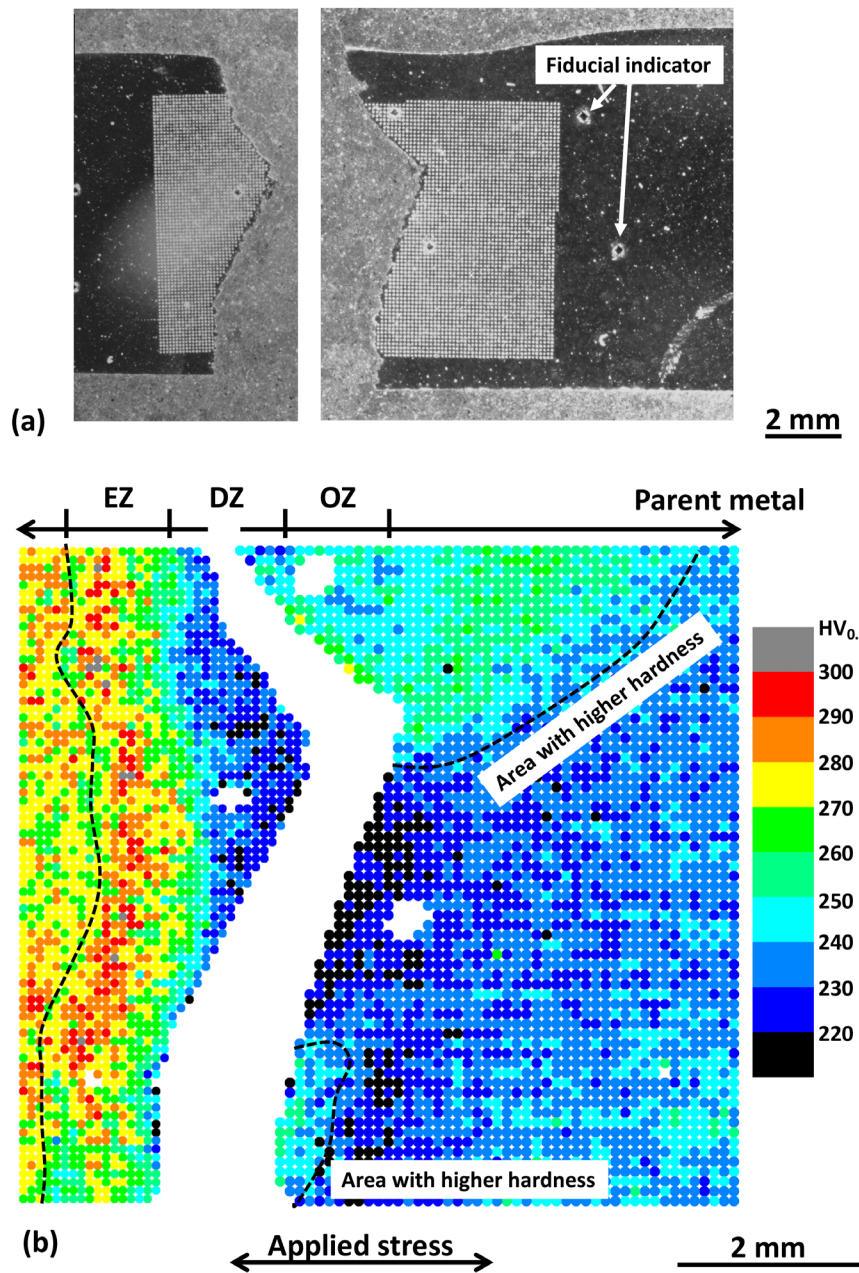
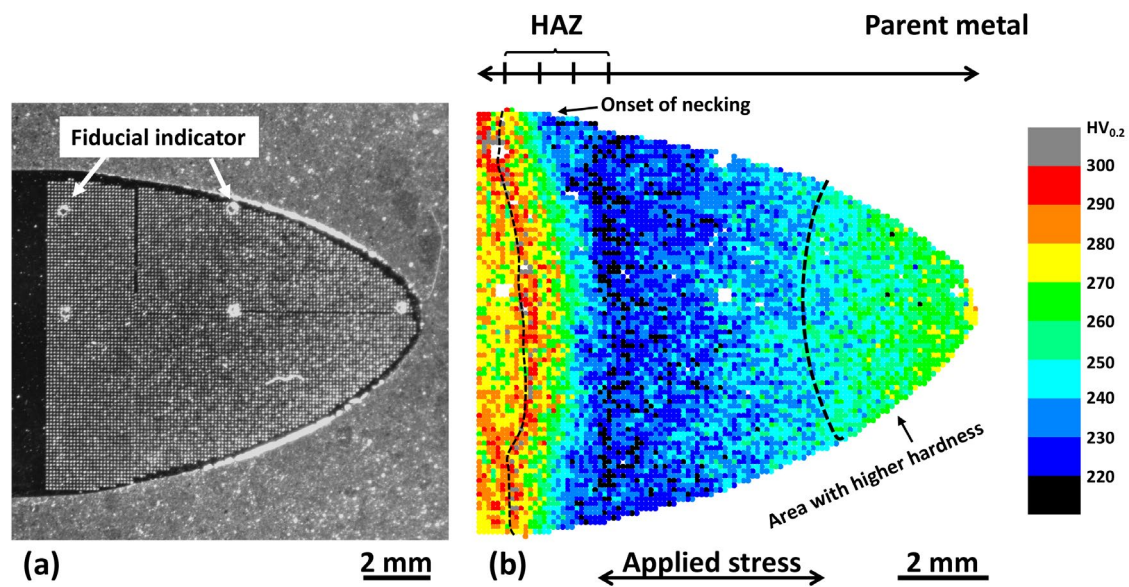


Figure 6. (a) Photographs showing the cross-section of a creep ruptured cross-weld specimen after creep testing at 650°C and 160 MPa for 705 hours prior to hardness mapping analysis. (b) A hardness map showing the variation of hardness in the region of analysis.

Figure 6b shows that the hardness of the weld metal ranges between 238 and 299 HV<sub>0.2</sub> with an average hardness measuring  $274 \pm 9$  HV<sub>0.2</sub>, whereas the hardness of the parent

metal is in the range of 221-258 HV<sub>0.2</sub> with an average value obtained at 236±6 HV<sub>0.2</sub>. The hardness in the HAZ decreases from 312 HV<sub>0.2</sub> to 205 HV<sub>0.2</sub> with distance from the fusion boundary. The rupture surface is located at ~1.0-2.5 mm from the fusion boundary with a zig-zag crack path. The rupture surface is aligned at ~90° to the principal stress direction close to the outer surface (bottom), whereas it is ~70° and ~45° to the principal stress direction in the centre and close to the other side (top), respectively. The hardness in the regions extending from the portions at ~90° and ~45° is in the range of 232-253 HV<sub>0.2</sub> and 235-273 HV<sub>0.2</sub>, respectively. The hardness measured from the regions extending from the portion at ~70° to the principal stress direction is lower and in the range between 206 and 237 HV<sub>0.2</sub>. The angle of the rupture surface is mainly controlled by the microstructure of the weld and the local stress state during creep testing. However, it is also affected by the other factors including the surface condition of the specimen and the experimental condition of creep test.

Hardness mapping analysis was further conducted on the creep ruptured specimen which was tested at 650°C and 200 MPa, Figure 7.





**Figure 7. (a) A photograph showing the cross-section of a creep ruptured cross-weld specimen after creep testing at 650°C and 200 MPa for 23 hours prior to hardness mapping analysis.**

The rupture surface is located at ~11 mm from the fusion boundary with substantial necking. The hardness measured from the weld and parent metals (Figure 7) is similar to the specimen ruptured at 160 MPa. The hardness of the weld metal is in the range between 253 and 314 HV<sub>0.2</sub> with an average value measuring 279±9 HV<sub>0.2</sub>, whereas the hardness of the parent metal is between 219 and 269 HV<sub>0.2</sub> with an average value obtained at 241±8 HV<sub>0.2</sub>. The hardness in the HAZ is similar to the specimen tested at 650°C and 160 MPa and is decreased from 320 to 205 HV<sub>0.2</sub> as the distance from the fusion boundary increases. The hardness in the regions close to the rupture surface is higher than the parent metal and increases to a maximum value of 285 HV<sub>0.2</sub>.

Fractographic examination was conducted on the rupture surfaces to understand the fracture behaviour of the creep exposed specimens. Figure 8 demonstrates the topography of the rupture surface in the specimens tested at 650°C/160 MPa and 650°C/200 MPa.

Figures 8b-8g demonstrate that the rupture surface in the specimen tested at 650°C and 160 MPa includes an intergranular rupture surface at ~90° to the principal stress direction and a ductile dimpled topography at ~70° and ~45°. The intergranular surface at ~90° is not similar to the characteristics of typical faceted surfaces formed by intergranular fracture [29], but it is covered by scale-like features that are possibly formed by oxidation (Figure 8g). The dimples in the region ~70°/~45° to the principal stress direction are typically 3-10 µm in diameter and occasionally associated with inclusion particles (e.g. Figure 8c), which is consistent with the existing report of plastic damage associated with

secondary phase particles [30]. The rupture surface of the specimen tested at 650°C and 200 MPa is composed of a dimpled central region in combination with a shear lip close to the outer surface (Figure 8h). Figure 8i demonstrates that the dimples in the central region are similar in size as compared to the specimen tested at 650°C and 160 MPa and occasionally associated with inclusions.

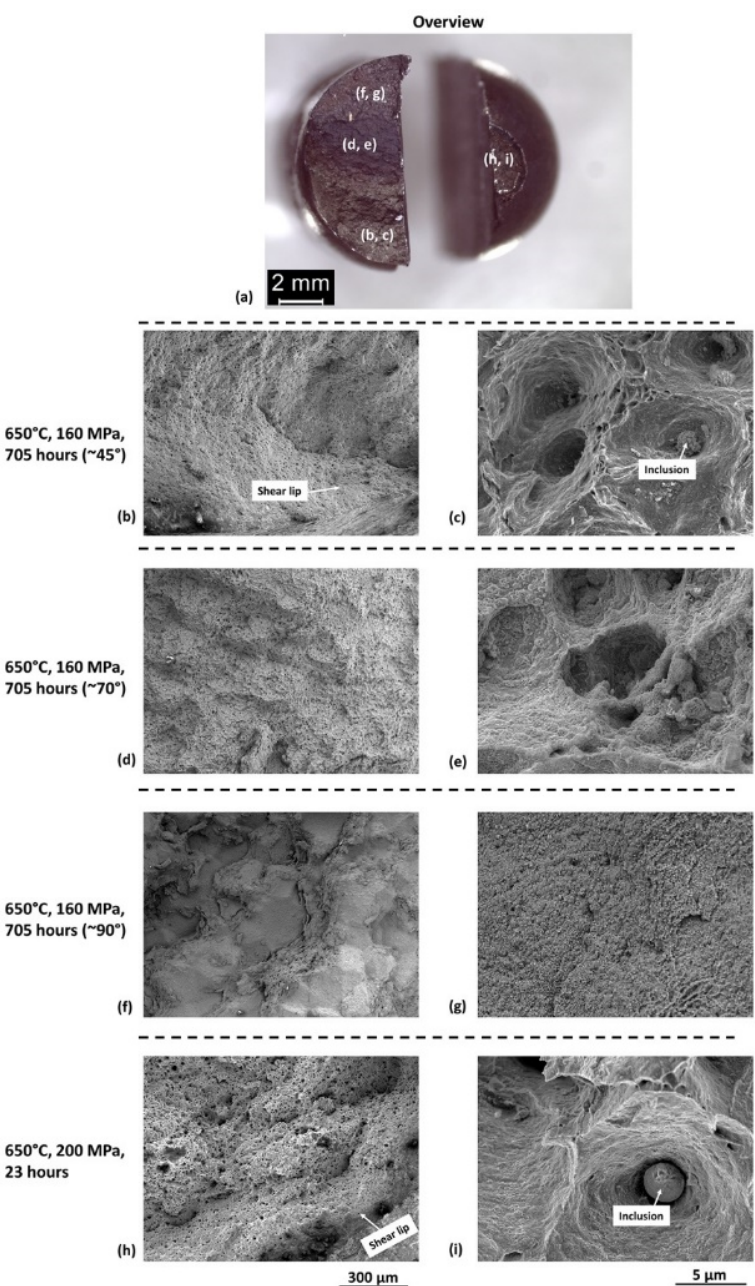


**Figure 8. (a) An optical overview of rupture surface in the specimens tested at (left) 650°C/160 MPa and (right) 650°C/200 MPa. Topography of the rupture surface is further detailed for the regions with an angle of (b, c) ~45°, (d, e) ~70° and (f, g) ~90° to the principal stress direction in the specimen tested at 650°C/160 MPa and (h, i) the rupture surface after creep testing at 650°C/200 MPa.**

Previous studies that were systematically conducted at various creep test conditions have revealed a variation in rupture behaviour from catastrophic HAZ failure occurring in the ‘Type IV’ zone, to ductile rupture of the parent metal against a decreasing testing temperature and/or an increasing stress level for the welds with a parent metal of similar materials [11,31]. This trend in creep rupture behaviour against the variation of creep test condition is consistent with the creep behaviour of IBN-1 steel welds between the tests conducted at 650°C and 160/200 MPa here. The IBN-1 weld tested at 200 MPa demonstrates similar creep behaviour to the IBN-1 parent materials from the identical industrial heat in tests at similar conditions, where dislocation climb acts as the dominant rate controlling factor for creep deformation [22]. However, the specimen tested at 650°C and 160 MPa demonstrates distinctively different creep rupture behaviour as indicated by an intergranular rupture surface located in the HAZ. Detailed metallographic examination is required to obtain an in-depth understanding of metallurgical causes for the occurrence of intergranular HAZ failure.

#### **3.4. The influence of HAZ microstructure on creep rupture**

EBSD mapping was conducted in local areas close to the rupture surface in the HAZ of the specimen tested at 650°C and 160 MPa, Figure 9.

Figure 9 clearly demonstrates the correlation between HAZ microstructure and the location of rupture surface. The surface portion at  $\sim 45^\circ$  to the principal stress direction is close to the boundary between the DZ and the OZ, whereas the portion at  $\sim 70^\circ$  is located within the DZ. The surface portion at  $\sim 45^\circ$  is transgranular and relatively straight (Figures 9a and 9b), whilst the surface portion at  $\sim 70^\circ$  is associated with both intergranular (Figure 9c) and transgranular (Figure 9d) characteristics. However, the surface portion at  $\sim 90^\circ$  is clearly intergranular and formed along the ‘necklace’ of pre-existing PAGBs as marked by the traces of refined grains  $<20\ \mu\text{m}$  in diameter (Figures 9e and 9f). The location of the intergranular surface portion has been confirmed in the region close to the boundary between the EZ and the DZ, with a distance of  $\sim 1.1\ \text{mm}$  from the fusion boundary. The presence of secondary damage was also observed in the intergranular region on pre-existing PAGBs and triple points (Figures 9f and 9g) in the area close to the rupture surface.

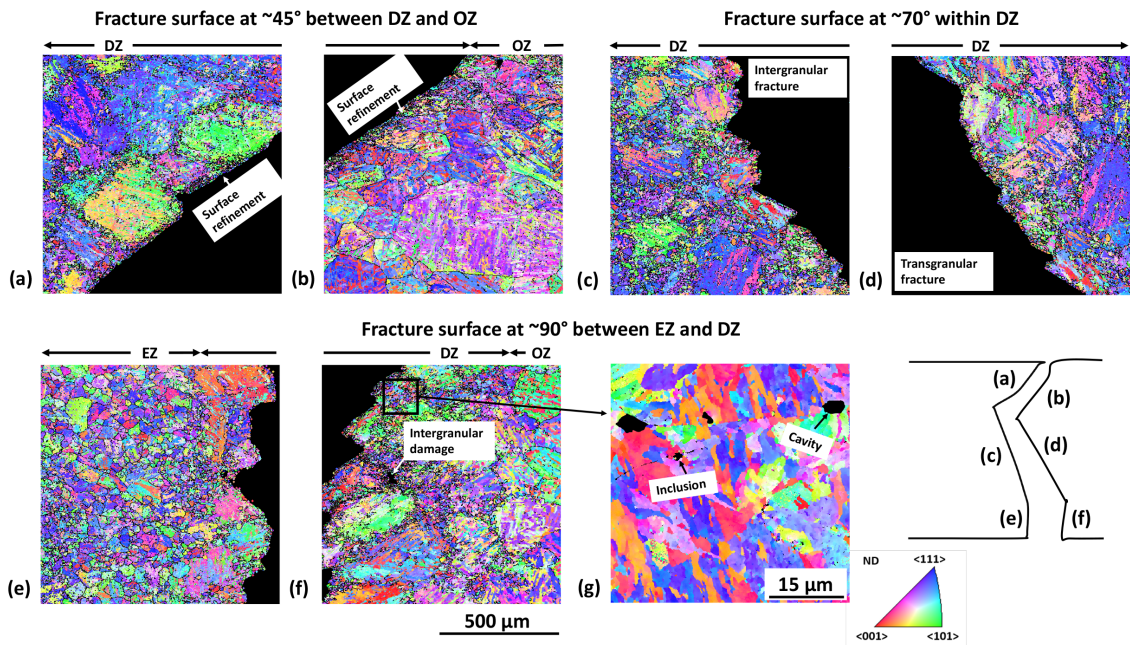


**Figure 9. EBSD maps showing the microstructure in the regions close to rupture surface at (a, b)  $\sim 45^\circ$ , (c, d)  $\sim 70^\circ$  and (e, f)  $\sim 90^\circ$  to the principal stress direction in the specimen tested at  $650^\circ\text{C}$  and 160 MPa. (g) An EBSD map collected at a higher resolution detailing the correlation between microstructure and secondary damage close to rupture surface. The grain boundaries with a misorientation range between  $20^\circ$  and  $50^\circ$  are outlined by solid lines. The inset indicate the location where the EBSD maps were collected.**

The initial microstructure in the HAZ of the as-fabricated IBN-1 weld was further investigated in detail to identify the cause of intergranular creep rupture from a metallurgical perspective. Figure 10 demonstrates the correlative micrographs obtained from the DZ regions in the as-fabricated weld at a similar distance from the fusion boundary as the location of the rupture surface using EBSD and ion induced SE imaging.

Figure 10a demonstrates a gradual transition between the EZ and DZ at  $\sim 1$  mm from the fusion boundary as indicated by the change in microstructure. One region (Region 1) selected for correlative EBSD/ion induced SE analysis is close to the boundary between the EZ and the DZ with a similar distance from the fusion boundary as the rupture surface (Figure 9) to compare with the microstructure in another region (Region 2) further away from the fusion boundary ( $\sim 1.3$  mm). EBSD mapping analysis (Figures 10b and 10d) reveals the elongated blocks that are a few microns in width within the martensitic substructure of the fine and coarse grains within the DZ, whereas the correlative ion induced SE micrographs (Figures 10c and 10e) demonstrate the precipitate particles that are preferentially distributed on substructure boundaries. Notably, the boundary of the refined grains formed along a pre-existing PAGB (e.g. Grain B) are consistently decorated by precipitate particles with a diameter of  $<150$  nm in Region 1 (Figure 10c),



whereas the boundary of the refined grains in Region 2 (e.g. Grain D) are decorated to a lesser extent (Figure 10d). This is attributed to an incomplete dissolution of the pre-existing precipitate particles in the regions further away from the fusion boundary due to a lower experienced peak temperature, which consumes the carbide forming elements in the matrix and mitigates a further formation of grain boundary precipitates as previously reported in Grade 92 steel weld [20].

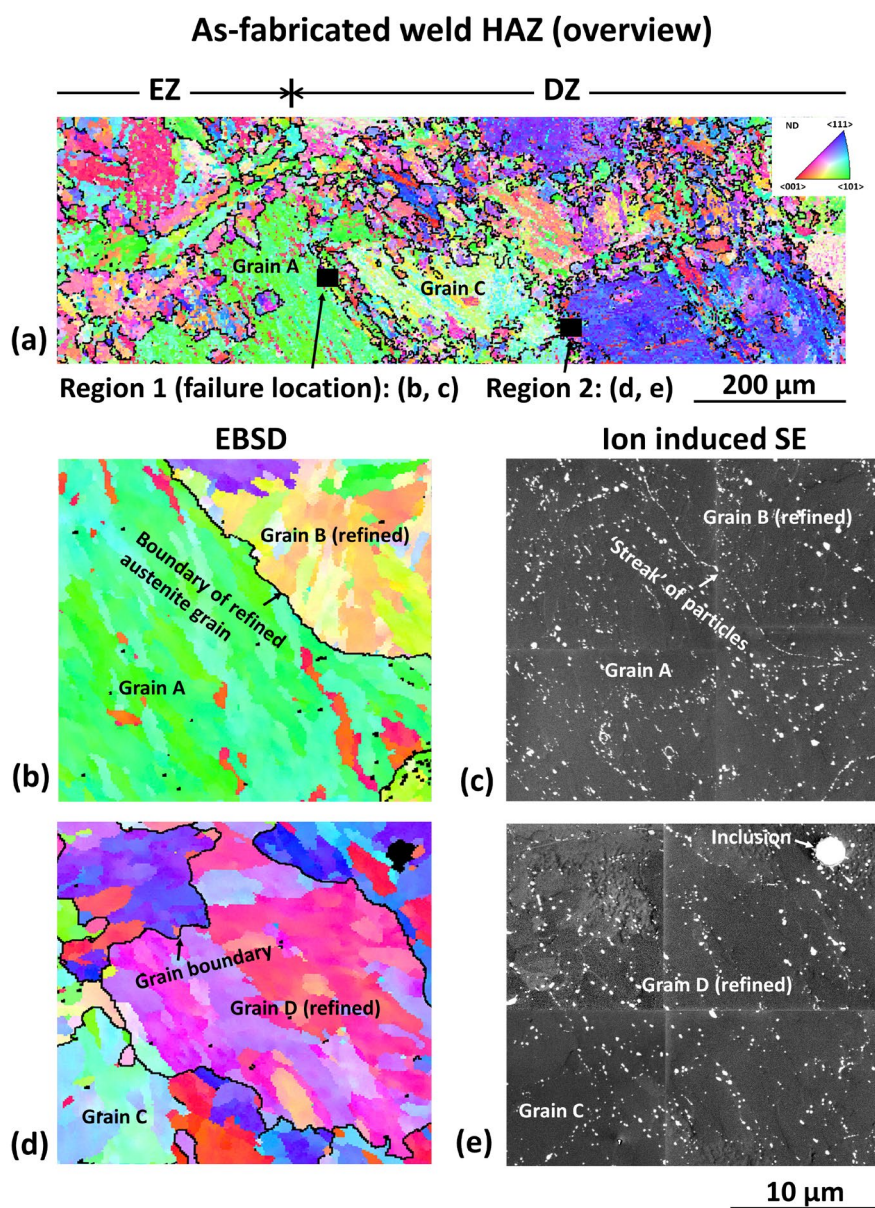
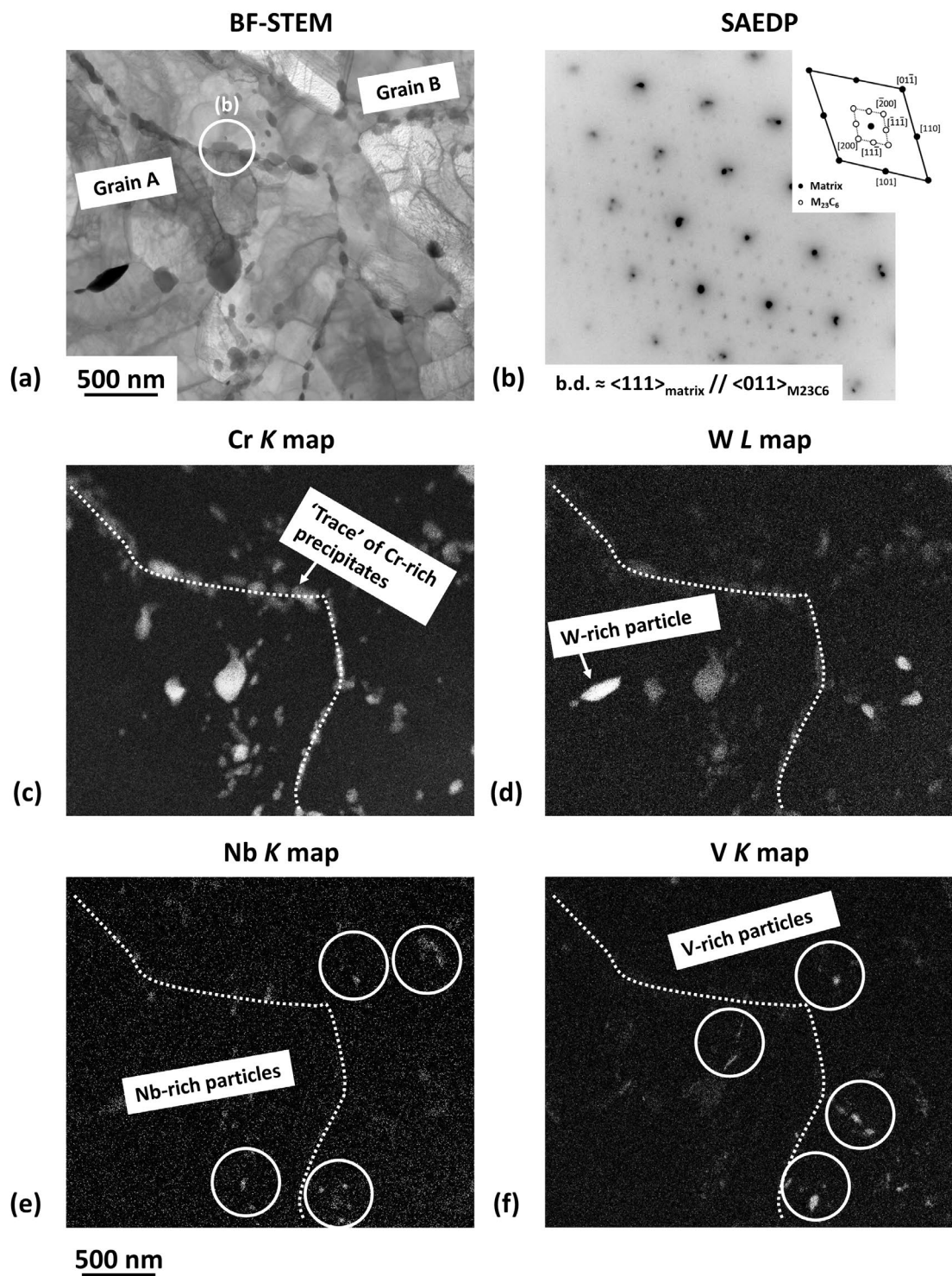


**Figure 10. (a) A large-scale EBSD map providing an overview of microstructure in the DZ with the regions of specific analysis indicated by black boxes. (b, d) EBSD and (c, e) ion induced SE micrographs of the martensitic substructure and the structure of precipitates in the regions at (b, c) 1.1 mm and (d, e) 1.3 mm from the fusion boundary. The boundary of small austenite grains on the ‘necklace’ of pre-existing PAGBs were revealed by a misorientation range of 20°-50°. Ion induced SE micrographs were inverted in grey scale for a clear visualisation of the precipitates as bright particles.**

The precipitates on the boundary of a refined grain (Grain B) in Region 1 were further extracted using the FIB lift-out technique for high-resolution analysis in TEM using SAED and STEM-EDX. Figure 11 displays a BF-STEM micrograph collected from the boundary of Grain B with the SAEDPs and EDX maps collected from precipitates and the surrounding matrix.

The martensitic substructure is predominantly composed of laths that are <1 µm in width in combination with a high density of dislocations within the lath interiors. The majority of the precipitate particles distributed on the boundaries of Grain B are <150 nm in diameter and have an FCC lattice structure similar to the  $M_{23}C_6$  carbides [32]. A crystal orientation relationship of  $\{011\}_{\text{precipitate}} // \{111\}_{\text{matrix}}$ ,  $\langle 111 \rangle_{\text{precipitate}} // \langle 011 \rangle_{\text{matrix}}$  was also confirmed between the precipitates and the matrix (Figure 11b). Figures 11c-11f further demonstrate that the precipitates distributed on the boundary of Grain B have a similar chemistry to the  $M_{23}C_6$  carbides that are abundant in Cr in combination with a minor level of W [33]. The presence of precipitate particles that are abundant in W or Nb/V was also observed at a minor level (Figures 11d-11f). The chemical compositions

455 of the W-rich and Nb/V-rich precipitates are similar to the chemistry of Laves and MX  
 456 carbonitrides [34,35], respectively.



457



**Figure 11. (a) A BF-STEM micrograph of the detailed martensitic microstructure in the region adjacent to the boundary of Grain B (Figure 10) and (b) an SAEDP collected from a precipitate particle with grey scale inverted for the visualisation of pattern. (c-f) Correlative EDX maps demonstrating the distribution of elements in the precipitates and the surrounding matrix.**

#### **4. DISCUSSION**

The dimpled rupture surface on the specimen tested at 650°C and 200 MPa is formed by ductile fracture due to significant stress concentration in the necked region, similar to that as previously observed in parent metal specimens [22]. However, the rupture behaviour of the IBN-1 weld tested at 650°C and 160 MPa is distinctively different and is marked by an intergranular rupture surface located within the HAZ. Based on detailed metallographic examinations of the specimens before and after creep exposure, the rupture surface generated at an applied stress of 160 MPa was found to be located in the region close to the boundary between EZ and DZ.

The EZ and DZ are distinctively classified by an evident transition in prior austenite grain morphology from an equiaxed microstructure to a duplex structure containing refined PAGs distributed on the initial PAGBs (Figure 10). These fine grains are likely to form via a diffusive transformation mechanism that is initiated from the PAGBs due to a lower energy for formation. This is evidenced by a preferential distribution of Cr-containing  $M_{23}C_6$  carbides on the boundary of these refined grains (Figure 10). This is caused by the segregation of carbide forming elements (e.g. Cr) on the boundaries as result of diffusion [36]. Similar observations were also obtained from a Fe-13%Cr-4%Ni-Mo martensitic

steel after diffusive austenitisation in the lower temperature regime (i.e. tempering at <680°C) as previously reported [36].

However, it is considered that the materials in the remaining area (i.e. close to the centre of PAGs) are associated with a displacive austenitisation process induced by the rapid heating rates experienced during welding. The existing observations of displacive austenitisation is comparatively limited for 9-12% Cr steels due to a relatively lower heating rate associated with typical manufacturing and heat treatment processes utilised for industrial applications [37]. However, fusion welding may facilitate the reaustenitisation of original parent metal in the weld HAZ via a diffusionless, displacive mechanism due to a high heating rate associated with weld thermal cycles that is typically >100°C/s as revealed in previous research [16,18]. The critical threshold of heating rate for the occurrence of displacive austenitisation has been determined to be ~400°C/s in a 0.15%C-5%Mn low alloy steel, whilst displacive austenitisation has been reported upon a heating rate of 5°C/s in a Fe-13%Cr-4%Ni-Mo steel [28,36].

The resultant microstructure formed by displacive austenitisation has been demonstrated in a previous study as a duplicated austenitic structure defined by high-angle PAGBs in combination with austenitic laths sharing similar crystal orientation formed within the PAG interiors [38]. The austenitic laths with a similar crystal orientation are formed within an individual PAG due to a crystallography memory effect that ‘reverses’ the orientation of  $\alpha/\alpha'$ -Fe matrix based on a Kurdjumov-Sachs orientation relationship [38].

In the current research, the microstructure observed from the central area within the PAG interiors in the DZ (Figures 3 and 9) is in strong agreement with the austenitic microstructure formed in a displacive manner as reported in [38]. This also explains the lack of high-angle boundaries within the interiors of pre-existing PAGs in the DZ as

highlighted by a range of misorientation of 20°-50°. Therefore, the duplex austenitic structure in the DZ is formed via a diffusive reaustenitisation process that gives rise to refined grains along the pre-existing PAGBs in combination with a displacive mechanism that reaustenitises the martensitic matrix within the PAG interior. This is consistent with the experimental observation as previously reported in another MarBN steel [26]. Upon further heating after austenitisation is completed, the displacively formed austenite is prone to recrystallisation due to a high density of dislocations in the microstructure as reported in [36,38]. This further explains the presence of an equiaxed austenitic structure in the regions closer to the fusion boundary as highlighted in the EZ area (Figures 3 and 9).

The martensite transformed from displacively formed austenite is commonly related with a higher dislocation density inherited from the initial austenitic microstructure as compared to the martensitic phases transformed from diffusively formed austenite [36,38]. This suggests a higher dislocation density in the martensitic matrix within the PAG interiors as compared to the intergranular regions showing a refined austenitic structure formed by diffusive phase transformation. Therefore, the intergranular regions along the PAGBs are more susceptible to damage formation by acting as the vulnerable sites in the microstructure. In addition, the correlative EBSD and ion induced SE analysis has revealed preferential formation of the  $M_{23}C_6$  carbides on the boundaries of diffusively formed austenite grains in the region close to the boundary between the EZ and DZ. This is consistent with the observation from a previous study on a Fe-1%Cr-0.6%C alloy that reveals the segregation of Cr accompanied with the migration of austenite grain boundaries during diffusive austenitisation [39]. The diffusion of carbide forming elements away from the pre-existing PAGBs further explains the scarcity of intergranular

$M_{23}C_6$  carbides in the areas between refined austenite grains. The depletion of precipitates on PAGBs may further contribute to a higher susceptibility of intergranular damage due to a lack of stabilisation effect provided by the grain boundary precipitates [33]. Figure 12 demonstrates a schematic diagram illustrating the critical metallurgical factors associated with the formation of intergranular damage in a duplex martensitic microstructure formed by a combination of diffusive and displacive mechanisms.

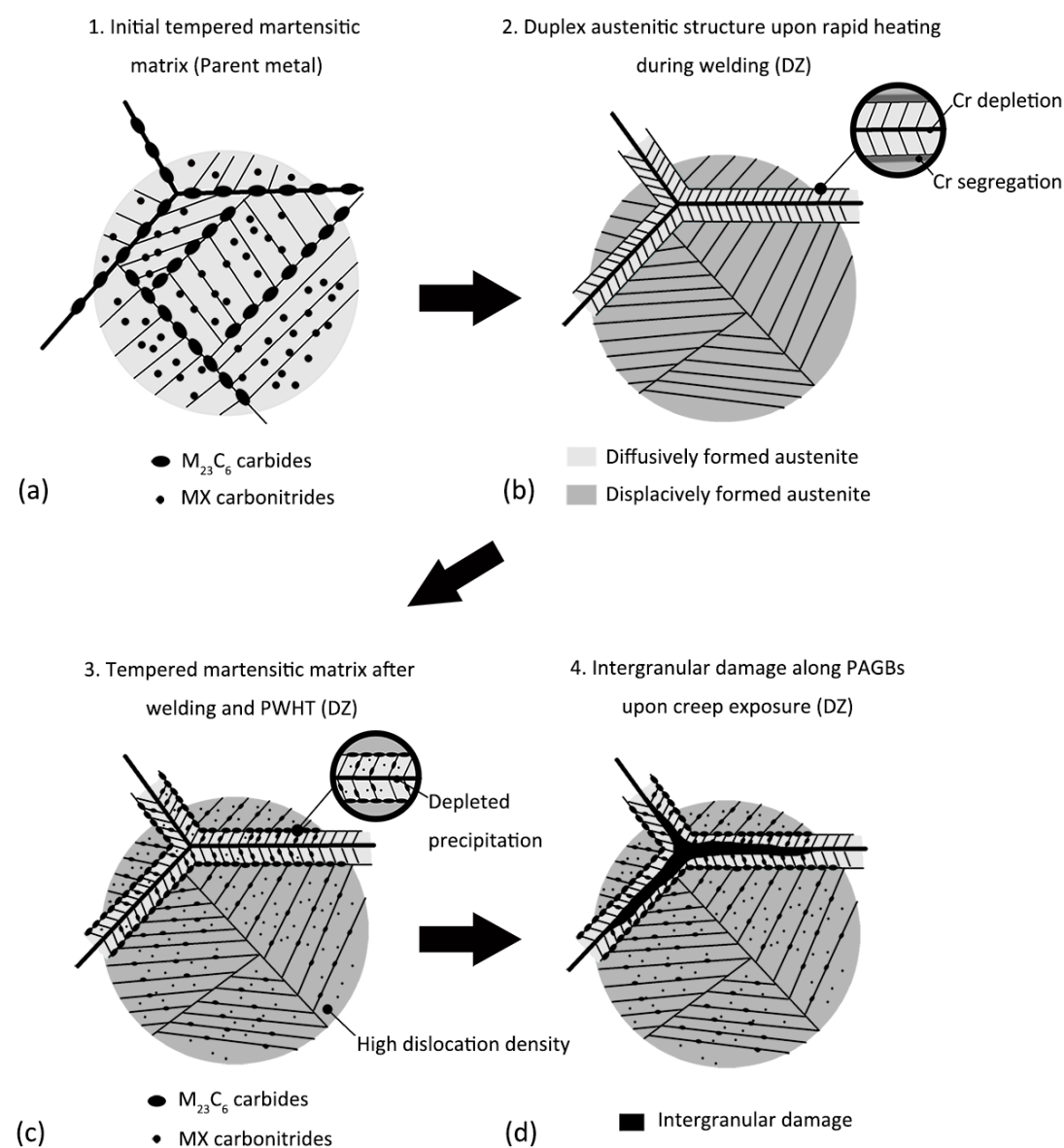


**Figure 12. A schematic diagram illustrating the formation of intergranular damage in the microstructure of DZ after reaustenitisation from the initial microstructure of the parent metal prior to PWHT.**

## **5. CONCLUSIONS**

The microstructural distribution in the HAZ of IBN-1 welds has been clearly determined and classified into three distinctive sub-regions as the Equiaxed Zone (EZ), the Duplex Zone (DZ) and the Over-tempered Zone (OZ) in the initial microstructure prior to creep exposure. The microstructural and mechanical characterisations conducted after short-term creep testing have further revealed an evident variation in creep behaviour between the welds tested at different stress levels and the bulk materials tested at identical conditions. From a mechanical point of view, a low creep resistance of the welds, as compared to the parent metal, has been observed. The SSCR values for the welds were found 26-fold higher than the parent metal, while the time to rupture was 14- to 18-fold shorter as compared to the parent metal.

Detailed fractography and metallography examinations revealed a ductile rupture occurred in the parent metal for the welds tested at a higher level of stress, whilst the welds tested at a lower stress demonstrated a failure location in the DZ microstructure close to the boundary with EZ. The initiation of such failure in IBN-1 welds was dominated by intergranular cracking along the pre-existing initial PAGBs from the original microstructure of the parent metal. The areas along these PAGBs acted as vulnerable sites in a tempered martensitic matrix transformed from an austenitic microstructure formed by a combination of diffusive and displacive mechanisms. In particular, the intergranular regions were associated with higher damage susceptibility

due to a relatively lower strength as compared to the matrix within the PAG interiors and a lack of precipitates on the PAGBs.

## **6. ACKNOWLEDGMENTS**

This work was supported by the Engineering and Physical Sciences Research Council (<https://www.epsrc.ac.uk/>) through the IMPULSE project (grant number: EP/N509991/1). The authors gratefully acknowledge the following partners for their valuable contributions: Doosan Babcock, GE Power, Uniper Technologies, Metrode Products, Goodwin Steel Castings and Wyman-Gordon. Specific acknowledgments to Dr Paul Robb (Doosan Babcock) for providing the test material and welding procedure. The authors also acknowledge use of facilities within the Loughborough Materials Characterisation Centre.

## **7. DATA AVAILABILITY**

The raw/processed data required to reproduce these findings cannot be shared at this time as the data also forms part of an ongoing study.

## **8. REFERENCES**

- [1] M. Taneike, F. Abe, K. Sawada, Creep-strengthening of steel at high temperatures using nano-sized carbonitride dispersions, *Nature*. 424 (2003) 294–296.
- [2] R. Viswanathan, R. Purgert, U. Rao, Materials technology for advanced coal power plants, in: Proc. 1st Int. Conf. ‘Super-High Strength Steels’, Rome, Italy, 2005.
- [3] T. Hamaguchi, H. Okada, S. Kurihara, H. Hirata, M. Yoshizawa, A. Iseda, Microstructural Evaluation of 9Cr-3W-3Co-Nd-B Heat-Resistant Steel (SAVE12AD)

579 After Long-Term Creep Deformation, in: ASME 2017 Pressure Vessels and Piping  
580 Conference, American Society of Mechanical Engineers, 2017.

581 [4] S. Hollner, E. Piozin, P. Mayr, C. Caës, I. Tournié, A. Pineau, B. Fournier,  
582 Characterization of a boron alloyed 9Cr3W3CoVNbBN steel and further improvement  
583 of its high-temperature mechanical properties by thermomechanical treatments, J. Nucl.  
584 Mater. 441 (2013) 15–23.

585 [5] D.J. Allen, An investigation of the factors determining creep strength and  
586 ductility in Grade 92 steel, in: Kern, T. (ed.) 4th International ECCC Creep & Fracture  
587 Conference (ECCC 2017), Dusseldorf, 10-14th September. Dusseldorf: Steel Institute  
588 VDEh.

589 [6] P. Yan, Z. Liu, H. Bao, Y. Weng, W. Liu, Effect of tempering temperature on  
590 the toughness of 9Cr–3W–3Co martensitic heat resistant steel, Mater. Des. 54 (2014)  
591 874–879.

592 [7] F. Masuyama, M. Matsui, N. Komai, Creep rupture behavior of advanced 9-12%  
593 Cr steel weldment, Key Eng. Mater. 171 (1999) 99–108.

594 [8] V. Sklenička, K. Kuchařová, M. Svobodová, M. Kvapilová, P. Král, L. Horváth,  
595 Creep properties in similar weld joint of a thick-walled P92 steel pipe, Mater. Charact.  
596 119 (2016) 1–12.

597 [9] H.J. Schuller, L. Hagn, A. Woitscheck, Cracking in the Weld Region of Shaped  
598 Components in Hot Steam Pipe Lines–Materials Investigations, Der Maschinenschaden.  
599 47 (1974) 1–13.

600 [10] D.J. Abson, J.S. Rothwell, Review of type IV cracking of weldments in 9-12%  
601 Cr creep strength enhanced ferritic steels, Int. Mater. Rev. 58 (2013) 437–473.

602 [11] J.A. Francis, W. Mazur, H. Bhadeshia, Review Type IV cracking in ferritic  
603 power plant steels, *Mater. Sci. Technol.* 22 (2006) 1387–1395.

604 [12] J.D. Parker, Creep cavitation in CSEF steels, in: *Proc. Seventh Int. Conf. Adv.*  
605 *Mater. Technol. Foss. Power Plant*, 2013: p. 714.

606 [13] Y. Gu, Microstructural investigation of creep behaviour in Grade 92 power plant  
607 steels, Ph.D. thesis, 2017.

608 [14] Y. Liu, S. Tsukamoto, T. Shirane, F. Abe, Formation Mechanism of Type IV  
609 Failure in High Cr Ferritic Heat-Resistant Steel-Welded Joint, *Metall. Mater. Trans. A.*  
610 44 (2013) 4626–4633.

611 [15] K. Kimura, Y. Takahashi, Evaluation of long-term creep strength of ASME  
612 Grades 91, 92, and 122 type steels, in: *ASME 2012 Press. Vessel. Pip. Conf.*, American  
613 Society of Mechanical Engineers, 2012: pp. 309–316.

614 [16] M.S. L. Havelka, P. Mohyla, Thermal cycle measurement of P92 welded joints,  
615 in: *Proc. 23rd Int. Conf. Met. Mater.*, 2014.

616 [17] A.H. Yaghi, D.W.J. Tanner, T.H. Hyde, A.A. Becker, W. Sun, Abaqus Thermal  
617 Analysis of the Fusion Welding of a P92 Steel Pipe, in: *SIMULIA Cust. Conf.*, 2011:  
618 pp. 622–638.

619 [18] A.H. Yaghi, T.H. Hyde, A.A. Becker, W. Sun, Finite element simulation of  
620 welding and residual stresses in a P91 steel pipe incorporating solid-state phase  
621 transformation and post-weld heat treatment, *J. Strain Anal. Eng. Des.* 43 (2008) 275–  
622 293.

623 [19] X. Xu, G.D. West, J.A. Siefert, J.D. Parker, R.C. Thomson, Microstructural  
624 Characterization of the Heat-Affected Zones in Grade 92 Steel Welds: Double-Pass and  
625 Multipass Welds, *Metall. Mater. Trans. A.* 49 (2018) 1211–1230.



626 [20] X. Xu, G.D. West, J.A. Siefert, J.D. Parker, R.C. Thomson, The Influence of  
 627 Thermal Cycles on the Microstructure of Grade 92 Steel, *Metall. Mater. Trans. A.* 48  
 628 (2017) 5396–5414.

629 [21] J. Guo, X. Xu, M.A.E. Jepson, R.C. Thomson, Influence of weld thermal cycle  
 630 and post weld heat treatment on the microstructure of MarBN steel, *Int. J. Pres. Ves.*  
 631 *Pip.* 174 (2019) 13-24.

632 [22] A. Benaarbia, X. Xu, W. Sun, A.A. Becker, M.A.E. Jepson, Investigation of  
 633 short-term creep deformation mechanisms in MarBN steel at elevated temperatures,  
 634 *Mater. Sci. Eng. A.* 734 (2018) 491-505.

635 [23] L. Li, R. MacLachlan, M. a. E. Jepson, R. Thomson, Microstructural Evolution  
 636 of Boron Nitride Particles in Advanced 9Cr Power Plant Steels, *Metall. Mater. Trans.*  
 637 *A.* 44 (2013) 3411–3418.

638 [24] L.A. Giannuzzi, B.W. Kempshall, S.M. Schwarz, J.K. Lomness, B.I. Prenitzer,  
 639 F.A. Stevie, FIB Lift-Out Specimen Preparation Techniques, in: L.A. Giannuzzi, F.A.  
 640 Stevie (Eds.), *Introd. to Focus. Ion Beams Instrumentation, Theory, Tech. Pract.*,  
 641 Springer US, Boston, MA, 2005: pp. 201–228.

642 [25] Y. Li, K. Li, Z. Cai, J. Pan, X. Liu, P. Wang, Alloy design of welding filler  
 643 metal for 9Cr/2.25 Cr dissimilar welded joint and mechanical properties investigation,  
 644 *Weld. World.* 62 (2018) 1137–1151.

645 [26] F. Abe, M. Tabuchi, S. Tsukamoto, Metallurgy of Type IV fracture in advanced  
 646 ferritic power plant steels, *Mater. High Temp.* 28 (2011) 85–94.

647 [27] H. Kitahara, R. Ueji, N. Tsuji, Y. Minamino, Crystallographic features of lath  
 648 martensite in low-carbon steel, *Acta Mater.* 54 (2006) 1279–1288.

649 [28] N. Nakada, T. Tsuchiyama, S. Takaki, D. Ponge, D. Raabe, Transition from  
650 diffusive to displacive austenite reversion in low-alloy steel, *Isij Int.* 53 (2013) 2275–  
651 2277.

652 [29] C.L. Briant, S.K. Banerji, Intergranular failure in steel: the role of grain-  
653 boundary composition, *Int. Met. Rev.* 23 (1978) 164–199.

654 [30] J. Lin, Y. Liu, T.A. Dean, A review on damage mechanisms, models and  
655 calibration methods under various deformation conditions, *Int. J. Damage Mech.* 14  
656 (2005) 299–319.

657 [31] T. Sakthivel, M. Vasudevan, K. Laha, P. Parameswaran, K.S. Chandravathi, S.P.  
658 Selvi, V. Maduraimuthu, M.D. Mathew, Creep rupture behavior of 9Cr–1.8 W–0.5 Mo–  
659 VNb (ASME grade 92) ferritic steel weld joint, *Mater. Sci. Eng. A.* 591 (2014) 111–  
660 120.

661 [32] A. Baltusnikas, I. Lukosiute, R. Levinskas, Transformation kinetics of M23C6  
662 carbide lattice parameters in low alloyed steel, *Mater. Sci.* 16 (2010) 320–323.

663 [33] F. Abe, Precipitate Design for Creep Strengthening of 9% Cr Tempered  
664 Martensitic Steel for Ultra-supercritical Power Plants, *Sci. Technol. Adv. Mater. Sci.*  
665 *Technol. Adv. Mater.* 9 (2008) 13002–15.

666 [34] L. Cipolla, H.K. Danielsen, D. Venditti, P.E. Di Nunzio, J. Hald, M.A.J.  
667 Somers, Conversion of MX nitrides to Z-phase in a martensitic 12% Cr steel, *Acta*  
668 *Mater.* 58 (2010) 669–679.

669 [35] O. Prat, J. Garcia, D. Rojas, G. Sauthoff, G. Inden, The role of Laves phase on  
670 microstructure evolution and creep strength of novel 9% Cr heat resistant steels,  
671 *Intermetallics.* 32 (2013) 362–372.

672 [36] Y.Y. Song, X.Y. Li, L.J. Rong, D.H. Ping, F.X. Yin, Y.Y. Li, Formation of the  
673 reversed austenite during intercritical tempering in a Fe–13% Cr–4% Ni–Mo  
674 martensitic stainless steel, *Mater. Lett.* 64 (2010) 1411–1414.

675 [37] D. Richardot, J.C. Vaillant, A. Arbab, W. Bendick, The T92/P92 book  
676 Vallourec-Mannesmann tubes, (2000).

677 [38] Y. Song, X. Li, L. Rong, Y. Li, The influence of tempering temperature on the  
678 reversed austenite formation and tensile properties in Fe–13% Cr–4% Ni–Mo low  
679 carbon martensite stainless steels, *Mater. Sci. Eng. A.* 528 (2011) 4075–4079.

680 [39] N. Nakada, R. Fukagawa, T. Tsuchiyama, S. Takaki, D. Ponge, D. Raabe,  
681 Inheritance of dislocations and crystallographic texture during martensitic reversion into  
682 austenite, *ISIJ Int.* 53 (2013) 1286–1288.

683 [40] G. Miyamoto, H. Usuki, Z.-D. Li, T. Furuhashi, Effects of Mn, Si and Cr addition  
684 on reverse transformation at 1073 K from spheroidized cementite structure in Fe–0.6  
685 mass% C alloy, *Acta Mater.* 58 (2010) 4492–4502.

686

687

688 [1] M. Taneike, F. Abe, K. Sawada, Creep-strengthening of steel at high  
689 temperatures using nano-sized carbonitride dispersions, *Nature.* 424 (2003) 294–  
690 296.

691 [2] R. Viswanathan, R. Purgert, U. Rao, Materials technology for advanced coal  
692 power plants, in: *Proc. 1st Int. Conf. ‘Super-High Strength Steels’*, Rome, Italy,  
693 2005.

694 [3] T. Hamaguchi, H. Okada, S. Kurihara, H. Hirata, M. Yoshizawa, A. Iseda,  
695 Microstructural Evaluation of 9Cr-3W-3Co-Nd-B Heat-Resistant Steel

696 (SAVE12AD) After Long-Term Creep Deformation, (2017) V06AT06A064.

697 [4] S. Hollner, E. Piozin, P. Mayr, C. Caës, I. Tournié, A. Pineau, B. Fournier,  
698 Characterization of a boron alloyed 9Cr3W3CoVNbBN steel and further  
699 improvement of its high-temperature mechanical properties by thermomechanical  
700 treatments, J. Nucl. Mater. 441 (2013) 15–23.

701 [5] D.J. Allen, An investigation of the factors determining creep strength and  
702 ductility in Grade 92 steel, (2018).

703 [6] P. Yan, Z. Liu, H. Bao, Y. Weng, W. Liu, Effect of tempering temperature on the  
704 toughness of 9Cr–3W–3Co martensitic heat resistant steel, Mater. Des. 54 (2014)  
705 874–879.

706 [7] F. Masuyama, M. Matsui, N. Komai, Creep rupture behavior of advanced 9-12%  
707 Cr steel weldment, Key Eng. Mater. 171 (1999) 99–108.

708 [8] V. Sklenička, K. Kuchařová, M. Svobodová, M. Kvapilová, P. Král, L. Horváth,  
709 Creep properties in similar weld joint of a thick-walled P92 steel pipe, Mater.  
710 Charact. 119 (2016) 1–12.

711 [9] H.J. Schuller, L. Hagn, A. Woitscheck, Cracking in the Weld Region of Shaped  
712 Components in Hot Steam Pipe Lines—Materials Investigations, Der  
713 Maschinenschaden. 47 (1974) 1–13.

714 [10] D.J. Abson, J.S. Rothwell, Review of type IV cracking of weldments in 9-12%  
715 Cr creep strength enhanced ferritic steels, Int. Mater. Rev. 58 (2013) 437–473.

716 [11] J.A. Francis, W. Mazur, H. Bhadeshia, Review Type IV cracking in ferritic  
717 power plant steels, Mater. Sci. Technol. 22 (2006) 1387–1395.

718 [12] J.D. Parker, Creep cavitation in CSEF steels, in: Proc. Seventh Int. Conf. Adv.  
719 Mater. Technol. Foss. Power Plant, 2013: p. 714.

- 720 [13] Y.Gu, Microstructural investigation of creep behaviour in Grade 92 power plant  
721 steels, 2017.
- 722 [14] Y. Liu, S. Tsukamoto, T. Shirane, F. Abe, Formation Mechanism of Type IV  
723 Failure in High Cr Ferritic Heat-Resistant Steel-Welded Joint, *Metall. Mater.*  
724 *Trans. A.* 44 (2013) 4626–4633.
- 725 [15] K. Kimura, Y. Takahashi, Evaluation of long-term creep strength of ASME  
726 Grades 91, 92, and 122 type steels, in: *ASME 2012 Press. Vessel. Pip. Conf.*,  
727 American Society of Mechanical Engineers, 2012: pp. 309–316.
- 728 [16] M.S. L. Havelka, P. Mohyla, Thermal cycle measurement of P92 welded joints,  
729 in: *Proc. 23rd Int. Conf. Met. Mater.*, 2014.
- 730 [17] A.H. Yaghi, D.W.J. Tanner, T.H. Hyde, A.A. Becker, W. Sun, Abaqus Thermal  
731 Analysis of the Fusion Welding of a P92 Steel Pipe, in: *SIMULIA Cust. Conf.*,  
732 2011: pp. 622–638.
- 733 [18] A.H. Yaghi, T.H. Hyde, A.A. Becker, W. Sun, Finite element simulation of  
734 welding and residual stresses in a P91 steel pipe incorporating solid-state phase  
735 transformation and post-weld heat treatment, *J. Strain Anal. Eng. Des.* 43 (2008)  
736 275–293.
- 737 [19] X. Xu, G.D. West, J.A. Siefert, J.D. Parker, R.C. Thomson, Microstructural  
738 Characterization of the Heat-Affected Zones in Grade 92 Steel Welds: Double-  
739 Pass and Multipass Welds, *Metall. Mater. Trans. A.* 49 (2018) 1211–1230.  
740 doi:10.1007/s11661-017-4446-6.
- 741 [20] X. Xu, G.D. West, J.A. Siefert, J.D. Parker, R.C. Thomson, The Influence of  
742 Thermal Cycles on the Microstructure of Grade 92 Steel, *Metall. Mater. Trans.*  
743 *A.* 48 (2017) 5396–5414. doi:10.1007/s11661-017-4306-4.

- 744 [21] M.A.E.J. and R.C.T. J. Guo , X. Xu, INFLUENCE OF WELD THERMAL  
745 CYCLE AND POST WELD HEAT TREATMENT ON THE  
746 MICROSTRUCTURE OF MARBN STEEL, *Int. J. Press. Vessel. Pip.* (n.d.).
- 747 [22] A. Benaarbia, X. Xu, W. Sun, A.A. Becker, M.A.E. Jepson, Investigation of  
748 short-term creep deformation mechanisms in MarBN steel at elevated  
749 temperatures, *Mater. Sci. Eng. A.* (2018).
- 750 [23] L. Li, R. MacLachlan, M. a. E. Jepson, R. Thomson, Microstructural Evolution  
751 of Boron Nitride Particles in Advanced 9Cr Power Plant Steels, *Metall. Mater.*  
752 *Trans. A.* 44 (2013) 3411–3418. doi:10.1007/s11661-013-1642-x.
- 753 [24] L.A. Giannuzzi, B.W. Kempshall, S.M. Schwarz, J.K. Lomness, B.I. Prenitzer,  
754 F.A. Stevie, FIB Lift-Out Specimen Preparation Techniques, in: L.A. Giannuzzi,  
755 F.A. Stevie (Eds.), *Introd. to Focus. Ion Beams Instrumentation, Theory, Tech.*  
756 *Pract.*, Springer US, Boston, MA, 2005: pp. 201–228. doi:10.1007/0-387-23313-  
757 X\_10.
- 758 [25] Y. Li, K. Li, Z. Cai, J. Pan, X. Liu, P. Wang, Alloy design of welding filler metal  
759 for 9Cr/2.25 Cr dissimilar welded joint and mechanical properties investigation,  
760 *Weld. World.* 62 (2018) 1137–1151.
- 761 [26] F. Abe, M. Tabuchi, S. Tsukamoto, Metallurgy of Type IV fracture in advanced  
762 ferritic power plant steels, *Mater. High Temp.* 28 (2011) 85–94.
- 763 [27] H. Kitahara, R. Ueji, N. Tsuji, Y. Minamino, Crystallographic features of lath  
764 martensite in low-carbon steel, *Acta Mater.* 54 (2006) 1279–1288.
- 765 [28] N. Nakada, T. Tsuchiyama, S. Takaki, D. Ponge, D. Raabe, Transition from  
766 diffusive to displacive austenite reversion in low-alloy steel, *Isij Int.* 53 (2013)  
767 2275–2277.

- 768 [29] C.L. Briant, S.K. Banerji, Intergranular failure in steel: the role of grain-boundary  
769 composition, *Int. Met. Rev.* 23 (1978) 164–199.
- 770 [30] J. Lin, Y. Liu, T.A. Dean, A review on damage mechanisms, models and  
771 calibration methods under various deformation conditions, *Int. J. Damage Mech.*  
772 14 (2005) 299–319.
- 773 [31] T. Sakthivel, M. Vasudevan, K. Laha, P. Parameswaran, K.S. Chandravathi, S.P.  
774 Selvi, V. Maduraimuthu, M.D. Mathew, Creep rupture behavior of 9Cr–1.8 W–  
775 0.5 Mo–VNb (ASME grade 92) ferritic steel weld joint, *Mater. Sci. Eng. A.* 591  
776 (2014) 111–120.
- 777 [32] A. Baltusnikas, I. Lukosiute, R. Levinskas, Transformation kinetics of M23C6  
778 carbide lattice parameters in low alloyed steel, *Mater. Sci.* 16 (2010) 320–323.
- 779 [33] F. Abe, Precipitate Design for Creep Strengthening of 9% Cr Tempered  
780 Martensitic Steel for Ultra-supercritical Power Plants, *Sci. Technol. Adv. Mater.*  
781 *Sci. Technol. Adv. Mater.* 9 (2008) 13002–15. doi:10.1088/1468-  
782 6996/9/1/013002.
- 783 [34] L. Cipolla, H.K. Danielsen, D. Venditti, P.E. Di Nunzio, J. Hald, M.A.J. Somers,  
784 Conversion of MX nitrides to  $\epsilon$ -Z-phase in a martensitic 12% Cr steel,  
785 *Acta Mater.* 58 (2010) 669–679.
- 786 [35] O. Prat, J. Garcia, D. Rojas, G. Sauthoff, G. Inden, The role of Laves phase on  
787 microstructure evolution and creep strength of novel 9% Cr heat resistant steels,  
788 *Intermetallics.* 32 (2013) 362–372.
- 789 [36] Y. Song, X. Li, L. Rong, Y. Li, The influence of tempering temperature on the  
790 reversed austenite formation and tensile properties in Fe–13% Cr–4% Ni–Mo  
791 low carbon martensite stainless steels, *Mater. Sci. Eng. A.* 528 (2011) 4075–

792           4079.

793   [37]   D. Richardot, J.C. Vaillant, A. Arbab, W. Bendick, The T92/P92 book Vallourec-

794           Mannesmann tubes, (2000).

795   [38]   N. Nakada, R. Fukagawa, T. Tsuchiyama, S. Takaki, D. Ponge, D. Raabe,

796           Inheritance of dislocations and crystallographic texture during martensitic

797           reversion into austenite, *Isij Int.* 53 (2013) 1286–1288.

798   [39]   G. Miyamoto, H. Usuki, Z.-D. Li, T. Furuhashi, Effects of Mn, Si and Cr addition

799           on reverse transformation at 1073 K from spheroidized cementite structure in Fe–

800           0.6 mass% C alloy, *Acta Mater.* 58 (2010) 4492–4502.

801